Long-term performance and durability of Ir/B$_4$C multilayer x-ray mirrors: focusing on composition, structure, and reflectivity properties

Atefeh Jafari,[a,*] Desiree D. M. Ferreira,[a] Shima Kadkhodazadeh,[b] Takeshi Kasama,[b,†] Sonny Massahi,[a] Sara Svendsen,[a] Lan M. Vu,[a] Peter L. Henriksen,[a] Zoltàn M. Balogh,[b] Michael Krumrey,[c] Levent Cibik,[c] Finn E. Christensen,[a] and Brian Shortt[d]

[a]Technical University of Denmark, DTU Space, Lyngby, Denmark
[b]Technical University of Denmark, DTU Nanolab, Lyngby, Denmark
[c]Physikalisch-Technische Bundesanstalt, Berlin, Germany
[d]European Space Agency, Noordwijk, The Netherlands

Abstract. Multilayer (ML) thin film coatings have shown promise in achieving hard x-ray nanofocusing with high reflectivity and high resolution. The chemical, structural, and long-term stability of Ir/B$_4$C MLs, which are of great interest to the synchrotron and astrophysics communities, are not yet fully understood. The evolution of the x-ray performance of Ir/B$_4$C ML mirrors was monitored over 5 years, and the chemical and structural properties were investigated in depth. Reflectivity scans reveal significant alteration in the energy range of 3.4 to 10 keV over this period. Furthermore, thickness and density degradation of B$_4$C layers were observed in scanning electron transmission microscopy results. The oxidation of B$_4$C occurs only for the top layers, whereas the buried B$_4$C layers go through various complex chemical modifications. The x-ray reflectivity model of Ir/B$_4$C structure was modified, based on the experimental findings, and resulted in good understanding of the long-term reflectivity performance of the x-ray mirror coatings. © *The Authors. Published by SPIE under a Creative Commons Attribution 4.0 Unported License. Distribution or reproduction of this work in whole or in part requires full attribution of the original publication, including its DOI.* [DOI: 10.1117/1.JATIS.6.3.034005]

1 Introduction

Reflecting optics with multilayer (ML) thin-film coatings, using various nanostructures and materials, are employed in various applications, including EUV lithography,[1] synchrotron radiation beamlines,[2,3] x-ray free-electron lasers,[4] and astronomical optics.[5,6] In order to enhance the performance of x-ray observatory telescopes, which detect x-ray emission in the universe (including clusters of galaxies, neutron stars, and black holes), further developments in these optical systems are required. The most important element in x-ray optics is the mirror system, which tunes the reflectivity range and the effective area. Missions, such as NASA's Chandra or ESA's XMM-Newton telescope launched in 1999, detect extreme objects that emit x-rays up to ~10 keV by utilizing iridium single layer x-ray mirror coatings in grazing incidence angle geometry.[7,8]

Single-layer mirror coatings can be replaced by MLs to enhance the reflectivity performance and to extend it to higher energies. For example, the recent NASA mission Nuclear Spectroscopic Telescope Array (NuSTAR) is working in the energy range from 3 to 79 keV by utilizing depth-graded MLs of Pt/C and W/Si.[9] Further investigations showed that significant improvement can be achieved at both low (below 2 keV) and high energies (around 9 keV) using MLs composed of high-Z/low-Z materials such as Ir with various carbide materials.[6,10,11]

---

*Address all correspondence to Atefeh Jafari, E-mail: atefeh.j87@gmail.com

This approach is currently under investigation for the upcoming Advanced Telescope for High ENergy Astrophysics (ATHENA) mission, expected to launch in the early 2030s. ATHENA MLs are designed to operate in the range of 0.1 to 10 keV.[11,12]

The highest reflectivity in a broad energy range has been achieved using boron carbide (B$_4$C) and silicon carbide (SiC) as the low-Z material.[10,11] Furthermore, the interesting optical and mechanical properties of B$_4$C make it a good candidate for a wide range of hard-coating applications.[13,14] Despite the excellent theoretical x-ray reflectivity (XRR) of Ir/B$_4$C ML mirrors,[15] experimental results revealed noticeable changes in reflectivity performance a short time after mirror deposition.[16–18] On the other hand, MLs of Cr/B$_4$C after 3 years[19] have shown stable reflective performance around 170 eV, while W/B$_4$C was found to be nearly stable at 8.047 keV over 2 years.[20] Discrepancies between the simulated and measured results have been described in our earlier reports.[11,21] The studies of B$_4$C-based multilayers suggest that their XRR stability is not the same and varies by case. Parameters such as material combination and deposition techniques could play a crucial role; therefore, it is important to characterize the mirrors produced for specific long-term applications, for example, space applications with a desired lifetime of at least 5 years.

The stability and durability of such material combinations are being investigated.[18,21–23] However, this cannot be done without a good understanding of the real composition and structure of the materials on the surface, at depth, and in the interfaces. Investigating the defects and contamination of the mirror coating is also important. This information could help us to understand the nano(micro)structure of the coating, and ultimately improve and modify the reflectivity model based on experimental observations. In this work, we report on the long-term reflectivity performance, chemical composition, chemical modifications, and contaminant elements of Ir/B$_4$C ML mirrors.

2 Materials and Methods

2.1 Materials

Table 1 describes the samples and coating details of three Ir/B$_4$C ML samples with the specifications given in Table 2. These samples were chosen from the batch of test mirrors for the ATHENA mission. A pair of Ir/B$_4$C MLs, samples A and B, were selected for the long-term study. These sample have been coated in one run with identical coating designs.

Table 1 Three Ir/B$_4$C ML mirrors produced using the dc magnetron-sputtering chambers. These are test mirrors for the ATHENA mission. Samples A and B are twin samples, coated under the same conditions at the same time. The SPO[12] were used for sample substrates A and B and a silicon wafer was used for sample C, the so-called witness sample.

Sample	Original ID	Coating date	Chamber
A	SPO 64-01-25	February 2014	DTU Space
B	SPO 123-03-30	February 2014	DTU Space
C	cs00012	October 2018	Cosine B.V.

Table 2 Structural designs for the Ir/B$_4$C ML mirrors. All thicknesses are in nanometers. Γ refers to the ratio between the thickness of Ir and the d spacing, i.e., the total thickness of the Ir and B$_4$C layers together. In the case of samples A and B, a thick Ir layer (called top Ir layer) and a cap layer of B$_4$C (the topmost layer) are deposited on the other five bilayers. Sample C is composed of nine bilayers of 2.6 nm B$_4$C + 6.7 nm Ir.

Sample	Cap layer, B$_4$C	Top Ir layer	d_5	d_4	d_3	d_2	d_1	Γ	Coating design
A and B	8.0	17.0	11.0	9.5	8.0	6.5	5.0	0.6	Linear-graded ML
C	2.6	6.4	—	—	—	—	—	—	Bilayers ML

Samples A (original ID: 64-01-25) and B (original ID: 123-03-30) have been deposited in the dc magnetron sputtering chamber at DTU Space,[24] with a linear-graded structure of Ir and B_4C on silicon pore optics substrates (SPO). SPO substrates are designed based on commercially available Si wafers and will be used on the ATHENA mission.[12] Sample A was dedicated to destructive tests, such as electron microscopy (performed in 2018), while sample B has been used only for reflectivity measurements to avoid any possible surface damage related to the experiment such as beam exposure. Sample C, with original ID cs00012, was deposited on a silicon substrate at the dc magnetron-sputtering deposition facility at Cosine B.V.[25] All samples were stored under ambient conditions.

2.2 Characterization Techniques

X-ray reflectometry (XRR) is a powerful tool to determine the thickness, interface roughness, optical constants, and the density of the materials. XRR can be measured in a range of incident grazing angles or energies. The XRR angle scan, known as θ-2θ scans, was measured at 8.047 keV at room temperature (the characteristic lines of Cu-K_α) using the set up at DTU Space, presented in Fig. 1.

Energy scans were acquired between ~3.4 and 10 keV at the four-crystal monochromator beamline of the Physikalisch-Technische Bundesanstalt (PTB-FCM) using the electron storage ring BESSY II. The configuration of the set up is shown in Fig. 2 and also described in other reports.[26,27] The sample and detectors are in an ultrahigh-vacuum system.

We performed x-ray photoelectron spectroscopy (XPS) with Ar^+ ion etching to obtain information on the compositional structure from the surface to deep within the MLs. The XPS
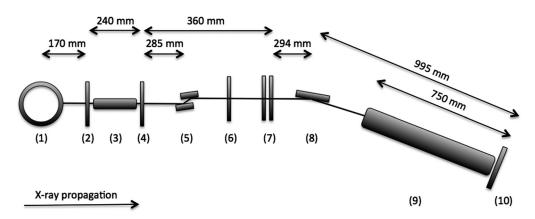

Fig. 1 The XRR experimental setup at DTU Space. (1) X-ray generator, (2) slit, (3) evacuated tube, (4) slit, (5) asymmetric cut Ge crystals, (6) attenuation filters, (7) beam shaping slits, (8) sample holder, (9) evacuated tube, and (10) position-sensitive detector.
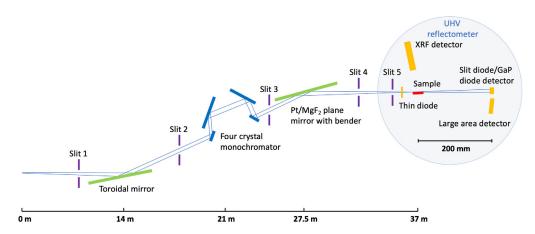

Fig. 2 The experimental setup for the XRR experiment on the PTB-FCM beamlime at BESSY II.

measurements were performed with monochromatized Al x-rays (1.4866 keV) using the XPS-ThermoScientific instrument at DTU Nanolab. Measurements were obtained using both survey and high-resolution spectra at different etching times.

The MLs were imaged in cross-sectional geometry using scanning transmission electron microscopy (STEM). Thin lamellae for STEM inspection were prepared by focused ion beam (FIB) milling in a Helios dual-beam instrument. Initially, the samples were protected from potential FIB-induced damage by depositing protective Pt layers. This was followed by FIB milling using a 30 kV Ga$^+$ ion beam. The cut-out lamellae were then lifted out and mounted on a TEM grid followed by final thinning to achieve electron transparency (<100 nm thick).

In addition to STEM imaging, electron energy loss spectroscopy (EELS) and energy-dispersive x-ray spectroscopy (EDS) were employed to probe the chemistry of the MLs, complementing the XPS measurements. STEM, EELS, and EDS measurements were performed in an FEI Titan instrument operated at 300 kV, with a probe size of ∼0.15 nm and energy resolution of 0.8 nm.

3 Results and Discussion

3.1 *XRR*

XRR angle scans at 8.047 keV of samples A and B were measured several times after the initial deposition in 2014 and are compared with the expected performance in Fig. 3(a). The simulated XRR curves are based on the designed structure as described in Table 2. The features (Kiessig fringes) of the measured reflectivity curves are close to the simulated curve, and results show nearly no reflectivity changes at this particular energy over 5 years. The last measurement result, sample B-2019 in the plot, had an improved angular resolution obtained using a set up developed at the PTB-FCM beamline. Energy scans of sample B, measured at a grazing angle of 0.6 deg, are shown in Fig. 3(b).

Results show discrepancies to the simulated curves and also reveal changes in regions below 7 keV and above 8.5 keV 5 years after the first measurement. Such changes are attributed to the B$_4$C cap layer oxidation.[21,22,28] In order to see the effect of this layer, we compared the measured
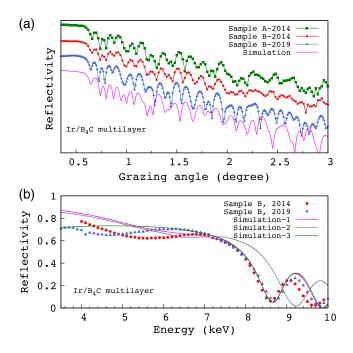

Fig. 3 XRR measurements of the Ir/B$_4$C ML, samples A and B measured at 8 keV facility at DTU Space. The XRR obtained in 2019 are measured at FCM-PTB beamline at BESSY II. (a) Angle scan XRR at 8.047 keV compared with expected performance based on designed structure shown in Table 2. (b) The energy scans at incident angle of 0.6 deg and three simulated curves, with B$_4$C cap layer (no. 1), with B$_2$O$_3$ cap layer (no. 2), and without the cap layer (no. 3) in ML structure with the design described in Table 2.

data with three simulated XRR results. Simulation no. 1 represents the reflectivity of the designed coating with an 8 nm B_4C cap layer, the nominal layer parameters given in Table 2. In simulation no. 2, the cap layer is replaced by an 8 nm B_2O_3 layer.[22,29] In simulation no. 3, with no cap layer, the effect of this layer on the reflectivity is shown. None of these three models agree with the XRR data neither in the experimental data acquired shortly after deposition in 2014, nor with the measurement of the same sample 5 years later in 2019.

Clearly, B_4C oxidization is not sufficient to explain the discrepancies and changes. In addition, assuming the worst-case scenario of the cap layer removal, e.g., due to experimental handling, the absence of that cap layer resulted in a significant decrease in reflectivity below ∼5 keV does not explain the variations that are seen in the measurements.

Furthermore, this could be related to coating degradation. Morawe et al. reported on the gradual transition of the B_4C layer in Pd/B_4C MLs that lead to entire degradation after 2 years.[49] Additional characterization tests have been performed in order to understand the real composition, layer structure, degradation, and also to investigate the reason for discrepancies between simulated and experimental results.

3.2 XPS

XPS survey and high-resolution scans were acquired for the B 1s, O 1s, C 1s, Ir 4f, Fe 2p, Si 2p, and Ar 2p electron shells with 130 iterations and steps of 10 s in etching time. The atomic concentration of each element was determined locally, presented in Fig. 4(a). XPS is surface-sensitive and its probing depth is ∼4 to 5 nm at 1486-eV photon energy. Interface roughness, deposition nonuniformity, and ion etching artifacts are known to be factors in the uncertainty in the XPS measurements when assessing the localization of the signals.

The depth-profile of sample A, presented in Fig. 4(a), shows that there is about 40% oxygen and 20% boron on the surface. These values decrease dramatically after 20 s etching so that the strong iridium peak emerges from the top iridium layer. This layer labeled no. 11 in the schematic drawing is shown in Fig. 4(b).

The iridium peak is suppressed by further etching mainly because the contribution of the elements present in the other layers, such as boron and carbon, are added to each scan, and this is due to the small thickness of the remaining layers compared to the probing depth. The sum of contributions of the three major elements (iridium, boron, and carbon) is about 90% for each etch time. Oxygen and iron dominate the remaining signals. Iron contamination arises from the coating chamber, and it has been found in other samples produced using the same facility. Carbon and oxygen peaks appear only where boron is at its highest concentration and iridium at the lowest, in other words in the B_4C layers. Iridium as a noble metal is highly resistant to oxidation and is expected to be immune to atmospheric attack.
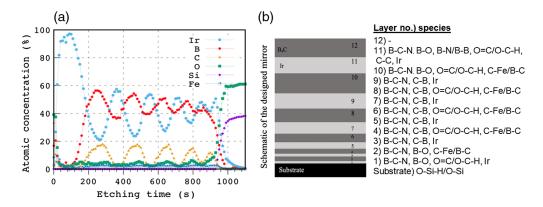

Fig. 4 Sample A XPS results. (a) Concentration quantification of selective elements for sample A (Ir/B_4C ML SPO 64-01-25) using XPS depth profiling. (b) Schematic of the ML mirror SPO 64-01-25 and the main bonds detected in each layer together with a list of the identified peaks in each scan, positions, and assignments. The relative thickness variation shown in the figure does not represent the designed or measured results and is drawn arbitrarily, for clarity.
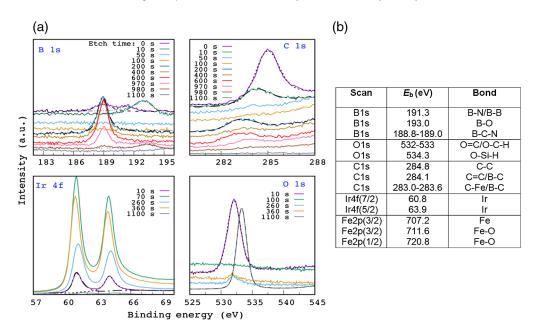
(a)

(b)

Scan	E_b (eV)	Bond
B1s	191.3	B-N/B-B
B1s	193.0	B-O
B1s	188.8–189.0	B-C-N
O1s	532–533	O=C/O-C-H
O1s	534.3	O-Si-H
C1s	284.8	C-C
C1s	284.1	C=C/B-C
C1s	283.0–283.6	C-Fe/B-C
Ir4f(7/2)	60.8	Ir
Ir4f(5/2)	63.9	Ir
Fe2p(3/2)	707.2	Fe
Fe2p(3/2)	711.6	Fe-O
Fe2p(1/2)	720.8	Fe-O

Fig. 5 High-resolution XPS spectra for sample A together with the list of peak positions and assignments. Different types of dashed lines show fit curves of different species.

A qualitative analysis of the high-resolution XPS scans was carried out to investigate the local chemical bonding of sample A. A summary of identified bonds is listed in Fig. 4(b), obtained from the high-resolution XPS scans. Figure 5(a) focuses on the detection of boron, carbon, iridium, and oxygen bonds. Peak positions and assignments are also listed in Fig. 5.

The two broad features of the B 1s signal from the surface, centered at 192.8 and 191.3 eV, are assigned to B—O bonds in the B$_2$O$_3$ environment[30–32] and some other oxide-related species.[33,34] These features re-emerge in the vicinity of the silicon oxide layer of the substrate (see scan 980s of the B 1s spectrum). The broad feature at 188.8 eV can be associated with B—C bonds,[33–35] and B—C—N bonds.[36] The intensity of this peak varies from the top to the bottom layers (etch times 200 s to <1000 s). The main B 1s component in the B$_4$C environment is expected to be around 188.3 eV.[37–39] Various boron components related to B$_4$C, boron-depleted boron carbide or elemental boron, and boron oxide have also been found in other magnetron-sputtered boron carbide films.[39]

In the C 1s scans, the graphite sp^3-bonded amorphous carbon states, with peak position of 284.8 eV, are observed at the surface and this peak shifts to 284.1 eV in the buried layers. This is attributed to sp^2 hybridized carbon.[34,36,40,41]

The broad peaks are overlapping features from the C—Fe at 283.3 eV and the C—B bond. The same gradual shift of the C 1s signal was observed in boron carbide films by Ronning et al.[42] B$_4$C-related C 1s features are expected at 282.7 and 284.0 eV, but the latter peak does not show up in our scans.

The O 1s peaks are observed in the range 532 to 533 eV. The gradual shift from 533 to 532 eV illustrates transition from single to double bonding in different layers in the sample.[34,43] The majority of the peaks belonging to the mid-layers is centered around 532.1 eV, associated with double bonding of oxygen. These signals could be due to the presence of carbonates.[43] On the other hand, the feature around 533 eV has been reported in several other works and either belongs to the O—B bonding in a B$_2$O$_3$ environment or C—OH/C—O—C bonds.[34,43,44] However, it is very difficult to assign the O 1s signals to one specific oxide environment as the peaks overlap. This is why more than one species or bond has been associated with this peak. Wessling et al. linked the 533-eV signal to the presence of water. The sharp peak at 534.3 is related to Si—O—H bonds on the surface of the substrate.[45] The Ir 4f scans reveal doublets with peaks centered at 60.9 and 64.0 eV, which are the Ir 4f(7/2) and Ir 4f(5/2) features in a metal iridium environment.[46,47]

Analysis of high-resolution XPS scans reveals evidence of boron oxidization in the top layer, in agreement with other reports.[18,28] Various forms of boron and carbon bonds exist in all the B$_4$C
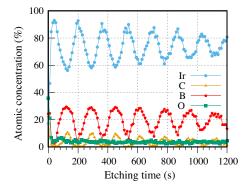
Fig. 6 XPS depth profile for sample C.

layers, indicating a more complex composition than the expected B$_4$C. No clear signature of a pure B$_4$C environment can be seen in the B 1s and C 1s signals. This can be explained in two ways: immediate decomposition of the sputtered B$_4$C leaving the target during the deposition on the substrate or gradual decomposition over 5 years.

The XPS results of sample C show similar evidence of boron oxide in the B$_4$C cap layer. The uniform distribution of precursor elements is visible in the depth-profile plot of sample C shown in Fig. 6. A boron-to-carbon ratio of ∼3.4(1) is determined in both samples A and C. The iron contamination is less in sample C, but the oxygen contamination occurs in all layers. The oxide-related features are expected only on the top layers because of the hydrocarbon overlayer and exposure to air, thus the source of oxygen throughout the buried layers is not clear.

3.3 *STEM*

Figure 7 shows cross-sectional bright-field scanning transmission electron microscopy (BF-STEM) images of sample A, recorded 4 years after the deposition date. The images show 11 layers, including six iridium and five B$_4$C layers, between the substrate and the protective Pt layer. The protective layer has been deposited prior to STEM inspection after 4 years of ambient exposure.

The B$_4$C cap layer in the sample cannot be seen here, possibly due to damage during the FIB milling process and also long-term instability of the material. Zooming in, the images reveal high levels of roughness at the interfaces. The observed interface roughness can also be due to chemical intermixing and diffusion at the interfaces. The average thickness of the layers, which are measured based on the intensity profile of the electron microscope images, are listed is Table 3.

The contrast between the layers arises from the difference in the atomic number of high-Z iridium and low-Z boron and carbon atoms. The contrast of the top B$_4$C layer is clearly different from the rest of B$_4$C layers, suggesting a different composition. A similar feature is found in the top B$_4$C layer of sample C shown by a red arrow in Fig. 8. The cap deposited B$_4$C layer can be
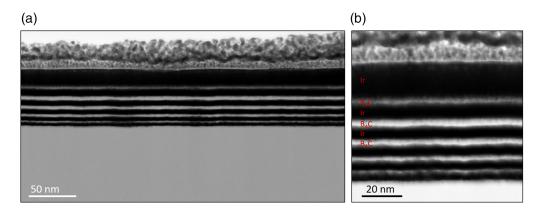
(a)　　　　　　　　　　　　　　　　　　　　(b)

Fig. 7 (a) BF-STEM images of sample A at different magnifications. (b) The black and white contrasts shown Ir and B$_4$C layers, respectively. Some of the layers are labelled.

Table 3 Derived fit parameters from energy scans of the Ir/B$_4$C ML mirror, sample B. The fit curves are shown in Fig. 13.

Measurement year	B$_4$C (cap.12)	Ir (11)	B$_4$C (10)	Ir (9)	B$_4$C (8)	Ir (7)	B$_4$C (6)	Ir (5)	B$_4$C (4)	Ir (3)	B$_4$C (2)	Ir (1)
					Thickness (nm)							
Design	8.0	17	4.4	6.6	3.8	5.7	3.2	4.8	2.6	3.9	2.0	3.0
STEM (2018)	Not-detected	17(1)	2(1)	8.0(5)	3.3(5)	5.8(5)	2.8(5)	5.0(5)	2.0(5)	3.5(5)	1.0(5)	3(1)
2014	5.5 + 3.3[a]	17.7	1.5 + 2.9[a]	6.0	5.1	6.0	5.7	2.5	2.8	3.3	2.7	2.5
2019	4.5 + 5.1[a]	19.1	5.5 + 4.2[a]	5.4	3.4	4.3	4.6	2.4	2.5	4.0	1.1	2.7
					Density (g/cm^3)							
2014	2.4 + 0.8[a]	22.4	1.0 + 0.6[a]	22.4	2.4	22.4	2.4	22.4	2.4	22.4	2.4	22.4
2019	1.6 + 0.4	22.4	0.9 + 0.8[a]	22.4	2.4	22.4	2.4	22.4	2.4	22.4	2.4	22.4
					Roughness (nm)							
2014	0.9	0.8	0.7	1.2	0.5	0.5	0.5	0.5	0.5	0.5	0.5	0.5
2019	0.9	0.8	0.7	1.2	0.5	0.5	0.5	0.5	0.5	0.5	0.5	0.5

Note: The italic parameters are the fitted ones resulting from the final fit to the reflectivity data. The density and thickness are the fitting parameters in those layers.
[a]In the best fit models, the top B$_4$C layers are replaced by two layers of boron carbide.
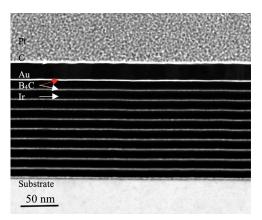
Fig. 8 STEM results of the Ir/B$_4$C ML sample C using BF mode. This sample has a protective Au layer added 10 months after the original deposition.

seen in this sample (C). Here, an additional protective layer of Au was sputtered on the sample prior to FIB milling in order to preserve the cap layer. More uniform coating and smoother interfaces can be seen in this sample. It is worth bearing in mind that the STEM inspection of sample C was performed 10 months after the deposition, compared to 4 years in sample A, and therefore, sample A has been more prone to long-term instability effects.

3.4 *EELS*

The chemistry of the samples was probed with 0.7 to 1 nm resolution using EELS. EELS scans were acquired for the boron K-edge, carbon K-edge, and iridium M-edge, with onsets at around 180, 285, and 2100 eV, respectively. The intensity of probed boron and carbon along with the STEM image intensity as functions of position across the layers in samples A and C are shown in Fig. 9. Results are obtained after plural scattering deconvolution and background subtraction. For both samples A and C, boron and carbon follow the same trend. A significant number of boron atoms present in iridium layers and this is significantly higher than for carbon, which is in the precursor and environmental contaminant element. Selective EELS spectra are shown in 10a.

Figure 10(a) shows several EELS spectra obtained from different positions along the MLs in sample A. A few reference spectra from the literature and database are shown in Fig. 10(b) for comparison. The iridium M edges are detected in the iridium layers and disappear completely in the B$_4$C layers. The boron signals in our EELS spectra do not vanish in the iridium layers, whereas the carbon signal does. The reproducibility of the results has been confirmed by repeating the experiment. Similar behavior is observed in sample C, where the boron signal is found in most of the iridium layers, see Figs. 9(b) and 11. Moreover, an excess C (or boron deficiency) is found in the top B$_4$C layers. One explanation for this observation is the high mobility of the
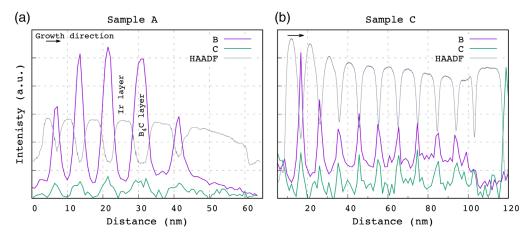

Fig. 9 Profile of boron and carbon intensities for Ir/B$_4$C (a) sample A and (b) sample C.
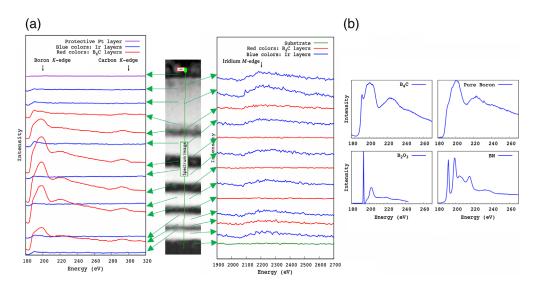
(a)

(b)

Fig. 10 EELS result for sample A. (a) The boron K, carbon K, and iridium M EELS edges from the line-scan measurements for sample A. (b) EELS spectra of B_4C, pure B, B_2O_3, and BN taken from EELS database.[48]

nonbonded boron atoms, leading to intermixing and diffusing over time. Another explanation can be the decomposition of B_4C during deposition, resulting in boron and carbon bonds in various forms, including nonbonded boron atoms. Interestingly, the boron K-edge at around 190 eV, recorded from different points across the layers in sample A, shows different fine structures, which indicates different bonding environments for boron. This is consistent with our XPS results. While most of the EELS-recorded B edges resemble B_4C and pure B, no evidence of boron oxide can be seen in the buried layers. It is important to remember that the cap B_4C layer has not been detected in this sample (A).
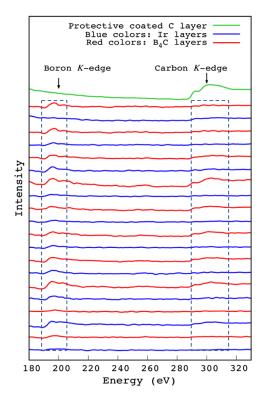

Fig. 11 The boron K and carbon EELS spectra for sample C.

Our results are in good agreement with resonant soft XRR results reported by Nayak et al. in which they show the presence of nonbonded boron in the B$_4$C ML and its effect on x-ray reflection. Their study also demonstrated that the B$_2$O$_3$ compound forms only when B$_4$C is on the top layer, while the buried layers, where B$_4$C is protected by other layers, remain oxide free.[18] Similar chemical instabilities have been noted in other B$_4$C MLs: C/B$_4$C[2], Pd/B$_4$C,[49] and W/Si/B$_4$C.[18] For example, in the study conducted by Rao et al.,[2] the presence of excess C in the boron carbide layer is associated with the diffusion of carbon atoms in the carbon layers and stoichiometric changes of the buried B$_4$C layers. Conversely, our EELS results indicate that carbon atoms are rather immobile, since we can only detect the boron signal in the iridium layers not the carbon signal. There was no oxygen signal observed from the top, boron carbide layer. If there was any oxidation of boron carbide, it must have been removed prior to inspection. Our quantitative analysis of the relative atomic ratios of boron to carbon gives a B:C ratio of 3.5(4) in the B$_4$C layers. This value is in good agreement with the 3.4(1) value obtained from XPS.

3.5 EDS

The acquired STEM-EDS scans revealed elements of iridium, boron, and carbon related to the coating as well as signals such as iron, copper, vanadium, cobalt, and argon, which arise mainly from the characterization environment. By comparing the EDS results with the XPS survey spectrum, the characterization environment's signals can be distinguished and excluded from the contaminated sample spectrum. Figure 12 shows the XPS survey and EDS spectra for samples A and C. For example, the iron signals are detected only for sample A in the XPS scan, while the EDS reveals iron in both samples from the microscope and the sample holder. Similar cases hold for vanadium, cobalt, and copper. The identified iron in sample A is contributed by both the characterization environment and the coating chamber. From XPS results, we know that iron is the major contaminant element of the sample. Sample C, which has been coated in a different chamber from samples A and B, is iron-free.

Light elements such as boron and oxygen are better probed by XPS, as can be seen in Fig. 12(a).

3.6 XRR Modeling

Based on our experimental findings from XPS and EELS, the boron carbide layer has a different stiochiometric signature than pure B$_4$C. Therefore, the use of the optical constants of B$_4$C for the XRR model is not correct. The samples studied a few years after the deposition show decomposition of the boron carbide into boron oxide in the layers closer to the surface and into other of B—C species in the buried layers.

Regardless of the reason for these changes, such chemical and structural instabilities lead to changes in the optical constants and densities, which, in turn, affect the reflectivity of the coated mirrors over time. This is demonstrated by the energy scans presented in Fig. 3(b). Note that this
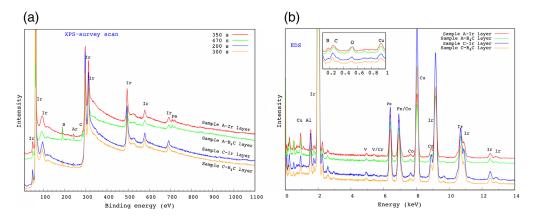

Fig. 12 Comparison of (a) XPS survey spectra and (b) TEM-EDS results for Ir and B$_4$C layers of samples A and C.
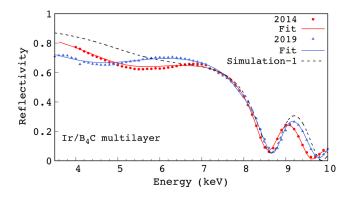
Fig. 13 Energy scan XRR of sample B, Ir/B_4C ML measured at BESSY II and corresponding best-fit models of the simulation shown in Fig. 3. The measurements were performed at 0.6 deg in 2014 and 2019.

variation is not detectable for angle scans at 8.047 keV. Making use of the results of our chemical characterization of the layers as input to the XRR model, considerably improved XRR models can be fitted to the experimentally measured ones, as shown in Fig. 13. The fit parameters are listed in Table 3.

XRR models must be defined with modified structures rather than the ideal model, i.e., pure B_4C and Ir with nominal densities from IMD.[50,51] Because of significant density variations in the top two B_4C layers, each layer is divided into two layers with different densities. Improving the fit models was not possible without varying the densities, in particular those of the B_4C layers. The density and thickness alteration of the top layers, i.e., nos. 12 and 10, are visible in STEM results. Degradation of the B_4C layers and the increased roughness of the interfaces could explain changes in the thickness of the buried B_4C layers. While our findings are consistent with earlier works,[2,18,49] it is important to note that the structural and chemical properties of the MLs could be dependent on the coating conditions, and the MLs may be stabilized through optimizing the deposition procedure and postprocessing, e.g., thermal annealing. On the other hand, our results for these Ir/B_4C MLs could be applied to other high-Z/low-Z thin films, if similar reflectivity instability is observed.

4 Conclusion

We have reached a good understanding of the Ir/B_4C MLs structure and the long-term reflectivity performance on Ir/B_4C coatings by utilizing characterization techniques XPS, STEM, EELS, EDS, and XRR.

Iron and oxygen were found as the main impurities. Iron was not present in sample C, which was coated in a different chamber than sample A. XPS and EELS investigations indicate that boron and carbon bonds decompose to various compounds with time. This could have been initiated during the deposition and/or evolved over an extended time period. Boron and carbon atoms have been found in various structural forms in buried boron carbide layers and at the interfaces. There was no oxidation state of boron found in buried layers. Boron has been shown to migrate into the Ir layers.

As the result of these changes, the XRR of Ir/B_4C MLs evolves with time, as seen over the 5-year time period reported here. This is confirmed by the improvements made to the modeled XRR spectra fit using the experimental energy scans of Ir/B_4C MLs, by adjusting the input parameters accordingly to match the measure layer structures and composition. This understanding can be generalized and applied to other low-Z/high-Z ML x-ray mirrors that show similar long-term changes in reflectivity performance.

Acknowledgments

assistance and Jonas Michael-Lindhard for his scientific guidance during the XPS measurements.

References

1. D. G. Stearns, R. S. Rosen, and S. P. Vernon, "Multilayer mirror technology for soft-x-ray projection lithography," *Appl. Opt.* **32**, 6952–6960 (1993).
2. P. N. Rao et al., "Microstructure and composition analysis of low-z/low-z multilayers by combining hard and resonant soft x-ray reflectivity," *J. Appl. Phys.* **119**(24), 245301 (2016).
3. A. T. Macrander and X. Huang, "Synchrotron x-ray optics," *Annu. Rev. Mater. Res.* **47**(1), 135–152 (2017).
4. M. Störmer, F. Siewert, and H. Sinn, "Preparation and characterization of B$_4$C coatings for advanced research light sources," *J. Synchrotron Radiat.* **23**, 50–58 (2016).
5. A. B. C. Walker et al., "Soft x-ray images of the solar corona with a normal-incidence cassegrain multilayer telescope," *Science* **241**(4874), 1781–1787 (1988).
6. D. Spiga, "Analytical evaluation of the x-ray scattering contribution to imaging degradation in grazing-incidence x-ray telescopes," *A&A* **468**(2), 775–784 (2007).
7. I. N. Evans et al., "The chandra source catalog," *Astrophys. J. Suppl. Ser.* **189**(1), 37 (2010).
8. F. Jansen et al., "XMM-Newton observatory*—I. The spacecraft and operations," *A&A* **365**(1), L1–L6 (2001).
9. F. A. Harrison et al., "The nuclear spectroscopic telescope array (NuSTAR) high-energy x-ray mission," *Astrophys. J.* **770**, 103 (2013).
10. D. D. M. Ferreira et al., "Coating optimization for the ATHENA+ mission," *Proc. SPIE* **8861**, 408–415 (2013).
11. D. D. M. Ferreira et al., "Design, development, and performance of x-ray mirror coatings for the ATHENA mission," *Proc. SPIE* **10399**, 1039918 (2017).
12. A. Jakobsen et al., "Preliminary coating design and coating developments for ATHENA," *Proc. SPIE* **8147**(1), 81470T (2011).
13. E. Pascual et al., "Boron carbide thin films deposited by tuned-substrate RF magnetron sputtering," *Diamond Relat. Mater.* **8**(2), 402–405 (1999).
14. S. Sasaki et al., "Thermoelectric properties of boron-carbide thin film and thin film based thermoelectric device fabricated by intense-pulsed ion beam evaporation," *Sci. Technol. Adv. Mater.* **6**(2), 181–184 (2005).
15. D. D. M. Ferreira et al., "ATHENA optimized coating design," *Proc. SPIE* **8443**, 84435L (2012).
16. P. Rao et al., "Thermal stability studies of ion beam sputter deposited C/B$_4$C x-ray multilayer mirror," *Thin Solid Films* **527**, 244–249 (2013).
17. P. Rao et al., "Investigation of composition of boron carbide thin films by resonant soft x-ray reflectivity," *Surf. Coat. Technol.* **334**, 536–542 (2018).
18. M. Nayak et al., "Determining chemically and spatially resolved atomic profile of low contrast interface structure with high resolution," *Sci. Rep.* **5**, 8618 (2015).
19. C. Burcklen et al., "Lifetime stability and microstructure properties of Cr/B$_4$C x-ray reflective multilayer coatings," *J. Nanosci. Nanotechnol.* **19**(1), 554–561 (2019).
20. P. S. Singam et al., "Thermal and temporal stability of W/B$_4$C multilayer mirrors for space-based astronomical applications," *J. Astron. Telesc. Instrum. Syst.* **4**(4), 1–8 (2018).
21. D. D. M. Ferreira et al., "Performance and stability of mirror coatings for the ATHENA mission," *Proc. SPIE* **10699**, 1069911 (2018).
22. S. Massahi, "Industrialization of the mirror plate coatings for the ATHENA mission," PhD Thesis, Technical University of Denmark (2019).
23. S. Svendsen et al., "Performance and time stability of Ir/SiC x-ray mirror coatings for ATHENA," *Proc. SPIE* **11119**, 111190G (2019).
24. A. Vickery et al., "Collimated magnetron sputter deposition for mirror coatings," *X-Ray Opt. Instrum.* 360–370 (2008).
25. S. Massahi et al., "Installation and commissioning of the silicon pore optics coating facility for the ATHENA mission," *Proc. SPIE* **11119**, 111190F (2019).

26. M. Krumrey, "Design of a four-crystal monochromator beamline for radiometry at BESSY II," *J. Synchrotron Radiat.* **5**, 6–9 (1998).

27. D. Fuchs et al., "High precision soft x-ray reflectometer," *Rev. Sci. Instrum.* **66**(2), 2248–2250 (1995).

28. S. Massahi et al., "The effect of nitrogen incorporation in boron carbide and iridium thin films," *Proc. SPIE* **10699**, 106993Y (2018).

29. P. N. Rao et al., "Depth-resolved compositional analysis of W/B₄C multilayers using resonant soft x-ray reflectivity," *J. Synchrotron Radiat.* **26**, 793–800 (2019).

30. O. Moon et al., "Temperature effect on structural properties of boron oxide thin films deposited by MOCVD method," *Thin Solid Films* **464–465**, 164–169 (2004).

31. J. Schreifels, P. Maybury, and W. Swartz, "X-ray photoelectron spectroscopy of nickel boride catalysts: correlation of surface states with reaction products in the hydrogenation of acrylonitrile," *J. Catal.* **65**(1), 195–206 (1980).

32. C. Wagner et al., "X-ray photoelectron spectroscopy of nickel boride catalysts: correlation of surface states with reaction products in the hydrogenation of acrylonitrile," *NIST Standard Reference Database 20, Version 3.4* (2003).

33. I. Jiménez et al., "Photoemission and x-ray-absorption study of boron carbide and its surface thermal stability," *Phys. Rev. B* **57**, 13167–13174 (1998).

34. L. Jacobsohn et al., "X-ray photoelectron spectroscopy investigation of boron carbide films deposited by sputtering," *Surf. Sci.* **572**(2), 418–424 (2004).

35. M. Polo et al., "Preparation of B-C-N thin films by r.f. plasma assisted CVD," *Diamond Relat. Mater.* **7**(2), 376–379 (1998).

36. M. Mannan et al., "Characterization of boron carbonitride (BCN) thin films deposited by radiofrequency and microwave plasma enhanced chemical vapor deposition," *Am. J. Appl. Sci.* **5**, 736–741 (2002).

37. W. Cermignani et al., "Synthesis and characterization of boron-doped carbons," *Carbon* **33**(4), 367–374 (1995).

38. K. Mustafa et al., "Kinetic investigation of chemical vapor deposition of B₄C on tungsten substrate," *AIChE J.* **52**(12), 4161–4166 (2006).

39. R. Soufli et al., "Optical constants of magnetron-sputtered boron carbide thin films from photoabsorption data in the range 30 to 770 ev," *Appl. Opt.* **47**, 4633–4639 (2008).

40. Y. Wang et al., "Nitrogen-doped porous carbon monoliths from polyacrylonitrile (PAN) and carbon nanotubes as electrodes for supercapacitors," *Sci. Rep.* **7**, 40259 (2017).

41. A. Furlan et al., "Structure and bonding in amorphous iron carbide thin films," *J. Phys.: Condens. Matter* **27**(4), 045002 (2015).

42. C. Ronning et al., "Ion beam synthesis of boron carbide thin films," *Surf. Coat. Technol.* **158-159**, 382–387 (2002).

43. D. Rosenthal et al., "Combined XPS and TPD study of oxygen-functionalized carbon nano-fibers grown on sintered metal fibers," *Carbon* **48**(6), 1835–1843 (2010).

44. J. Moulder and J. Chastain, *Handbook of X-Ray Photoelectron Spectroscopy: A Reference Book of Standard Spectra for Identification and Interpretation of XPS Data*, Physical Electronics Division, Perkin-Elmer Corporation, Waltham, Massachusetts (1992).

45. Y. L. Khung et al., "Formation of stable Si–O–C submonolayers on hydrogen-terminated silicon (111) under low-temperature conditions," *Beilstein J. Nanotechnol.* **6**, 19–26 (2015).

46. B. Wessling et al., "Reactively sputtered iridium oxide influence of plasma excitation and substrate temperature on morphology, composition, and electrochemical characteristics," *J. Electrochem. Soc.* **154**, F83–F89 (2007).

47. S. J. Freakley, J. Ruiz-Esquius, and D. J. Morgan, "The x-ray photoelectron spectra of Ir, IrO₂, and IrCl₃ revisited," *Surf. Interface Anal.* **49**(8), 794–799 (2017).

48. V. Serin et al., "Evidence for the solubility of boron in graphite by electron energy loss spectroscopy," *Carbon* **38**(4), 547–554 (2000).

49. C. Morawe, R. Supruangnet, and J.-C. Peffen, "Structural modifications in Pd/B₄C multi-layers for x-ray optical applications," *Thin Solid Films* **588**, 1–10 (2015).

50. D. L. Windt, "IMD-software for modeling the optical properties of multilayer films," *Comput. Phys.* **12**(4), 360–370 (1998).

51. B. Henke, E. Gullikson, and J. Davis, "X-ray interactions: photoabsorption, scattering, transmission, and reflection at E = 50-30,000 eV, Z = 1-92," *Atomic Data Nucl. Data Tables* **54**(2), 181–342 (1993).

Atefeh Jafari began her research career in x-ray optics at the Jülich Research Center and the European Synchrotron Radiation Facility (ESRF) as a PhD student in 2013. She received her PhD from the University of Liège. In 2017, she joined one of the European Space Agency's projects as a postdoctoral researcher at Denmark's National Space Institute, DTU Space. Her research interests include x-ray optics, light scattering, and nanomaterials. She is passionate about x-ray optics and the application of nanomaterials in advanced technology.

Shima Kadkhodazade received her PhD from the Department of Materials at Imperial College London in 2009. She has since been working at the Technical University of Denmark, first as a postdoc, and since 2017, as a senior researcher. Her research involves using transmission electron microscopy-based techniques to probe the nano- and atomic-scale structure of different materials, with the aim of understanding how they influence specific properties. She has contributed to 36 peer-reviewed articles.

Sara Svendsen is a PhD student in the Astrophysics and Atmospheric Physics Division at DTU Space. Her research is focused on development and characterization of x-ray reflective mirror coatings for the Athena telescope, parameter sensitivity in x-ray reflectometry, as well as ray tracing of x-ray optics.

Peter L. Henriksen is a PhD student in x-ray optics at DTU Space. His work includes beamline commissioning, reflective coating development, and optics optimization.

Michael Krumrey is head of the PTB Department for x-ray metrology. He designed and operated synchrotron radiation beamlines at BESSY I, ESRF and BESSY II and uses them for detector calibrations, x-ray reflectometry, and small-angle x-ray scattering as well as applications of x-rays for astrophysics and medicine. He studied physics in Berlin and Paris and received his diploma and PhD from the Technische Universität Berlin. He is the author or coauthor of about 140 refereed articles.

Biographies of the other authors are not available.